


Article

Photosynthetic Active Radiation, Solar Irradiance and the CIE Standard Sky Classification

Ana García-Rodríguez, Sol García-Rodríguez, Montserrat Díez-Mediavilla and Cristina Alonso-Tristán * 

Research Group Solar and Wind Feasibility Technologies (SWIFT), Electromechanical Engineering Department, Universidad de Burgos, 09006 Burgos, Spain; agrodriguez@ubu.es (A.G.-R.); solgr@ubu.es (S.G.-R.); mdmr@ubu.es (M.D.-M.)

* Correspondence: catristan@ubu.es or cristinaalonso.tristan@gmail.com

Received: 1 October 2020; Accepted: 9 November 2020; Published: 12 November 2020



Abstract: Plant growth is directly related to levels of photosynthetic photon flux density, Q_p . The improvement of plant-growth models therefore requires accurate estimations of the Q_p parameter that is often indirectly calculated on the basis of its relationship with solar irradiance, R_s , due to the scarcity of ground measurements of photosynthetic photon flux density. In this experimental campaign in Burgos, Spain, between April 2019 and January 2020, an average value of the Q_p/R_s ratio is determined on the basis of measurements at ten-minute intervals. The most influential factor in the Q_p/R_s ratio, over and above any daily or seasonal pattern, is the existence of overcast sky conditions. The CIE standard sky classification can be used to establish an unequivocal characterization of the cloudiness conditions of homogeneous skies. In this study, the relation between the CIE standard sky type and Q_p/R_s is investigated. Its conclusions were that the Q_p/R_s values, the average of which was $1.93 \pm 0.15 \mu\text{mol}\cdot\text{J}^{-1}$, presented statistically significant differences for each CIE standard sky type. The overcast sky types presented the highest values of the ratio, while the clear sky categories presented the lowest and most dispersed values. During the experimental campaign, only two exceptions were noted for covered and partial covered sky-type categories, respectively, sky types 5 and 9. Their values were closer to those of categories classified as clear sky according to the CIE standard. Both categories presented high uniformity in terms of illumination.

Keywords: photosynthetic active radiation; CIE standard skies; solar irradiance

1. Introduction

The portion of the solar spectrum that plant biochemical processes use in photosynthesis for converting light energy into biomass is a composite of wavelengths between 400 and 700 nm that are diffused within the visible light spectrum band (380–780 nm). These wavelength limits define the so-called photo-synthetically active radiation that covers both photon (Photosynthetic Photon Flux Density, Q_p ($\mu\text{mol}\cdot\text{s}^{-1}\cdot\text{m}^{-2}$)) and energy (PAR, Photo-synthetically Active Radiation, $\text{W}\cdot\text{m}^{-2}$) terms [1]. Usually, Q_p is recorded, and converted into energy units according to the McCree conversion factor of $4.57 \mu\text{mol}\cdot\text{J}^{-1} \pm 3\%$ depending on climatic factors [2]. Accurate PAR estimations are needed for modelling plant productivity and biomass production [3], natural illumination in greenhouses [4], plant physiology studies and leaf photosynthesis [5], to measure the productivity of forests [6], and to calculate the euphotic depth of the oceans [7]. Moreover, accurate PAR measurements have become central to the determination of deforestation and climate-change impacts on agriculture [8].

A global routine network for measuring PAR has yet to be established. This parameter is often indirectly calculated, due to the scarcity of PAR data, based on its relationship with global horizontal solar irradiance, R_s . The conventional PAR/R_s ratio falls between 0.45 and 0.50 [9]. Moon [10]

estimated the PAR/ R_s ratio at between 44% and 45% at sea level with a solar zenith angle of 30° over the horizon. Monteith [11] suggested that a constant ratio of 50% can be a good approximation for practical applications regardless of atmospheric aerosol and water vapor concentrations [12]. In terms of $\mu\text{mol}\cdot\text{J}^{-1}$, empirical relations [13] established Q_p/R_s ratios of between 2.1 and 2.9 $\mu\text{mol}\cdot\text{J}^{-1}$, depending on the location. The monthly Q_p/R_s average was calculated on a daily basis from experimental data [14] collected in an arid climate at between 2.02 and 2.19 $\mu\text{mol}\cdot\text{J}^{-1}$ and the mean daily value was 2.16 $\mu\text{mol}\cdot\text{J}^{-1}$. In Spain, Foyo-Moreno et al. [15] estimated a mean value of 1.95 $\mu\text{mol}\cdot\text{J}^{-1}$ a value close to other values from different locations [3,16]. Hu et al. [17] evaluated the Q_p/R_s ratio at many locations within China at between 1.75 $\mu\text{mol}\cdot\text{J}^{-1}$ and 2.30 $\mu\text{mol}\cdot\text{J}^{-1}$.

Several studies have been conducted to determine the relation between PAR/ R_s and different parameters. In some cases, significant relationships were found, but any dependencies on site geography, climatic and weather factors, seasonal trends, and both day length and diurnal effects were very slight and negligible for practical purposes [18]. Solar elevation has no significant effect on PAR/ R_s when greater than 10° [18,19].

The variations of this ratio with sky conditions have been studied to develop weather-dependent functions. Most studies have concluded that the PAR/ R_s ratio presents its highest values for cloud-covered skies [20,21]. This fact is attributable to cloud-related absorption and diffusion of solar radiation across different regions of the spectrum. The observed seasonal dependence of broad-band solar radiation is essentially caused by changes to turbidity, precipitable water, ozone, and clouds within the air masses at the location throughout the year [22]. The presence of water vapor increases the absorption effects within the infrared region of the spectrum, decreasing broadband solar irradiance levels to a greater extent than PAR. A secondary effect of the atmospheric water content is the enhancement of aerosol-related diffusion, which affects PAR more than broadband solar irradiance, R_s [4,23]. Some studies have proposed experimental models of PAR that include different parameters to take into account the atmospheric water vapor content, such as vapor pressure [16,24] and/or dewpoint temperature [4].

The definition of sky types (clear, overcast, and partly-cloudy) for this task take into account different combinations of meteorological variables, mainly the clearness index, k_t (ratio of global solar radiation to extraterrestrial solar radiation) [14,25–28]; k_t and relative sunshine, S , [29,30]; Perez's clearness index, ε , and sky brightness, Δ , [4,31], and types and extent of cloud cover [32]. However, the conclusions of a previous work [33] suggested that the use of meteorological variables or meteorological indices, showed limited results for sky classification. The use of meteorological indices for sky classification depends more on their availability than on their accuracy and various authors have used such indices (or combinations thereof) in different ways.

Sky classification is a complex problem, due in part to such abstract conceptual definitions as clear, partial cloudy, and overcast, as well as other intermediate ranges. The study of the dependence of any magnitude with respect to the type of sky firstly requires a standardized classification of the skies, to specify the atmospheric characteristics and illumination levels of each of the established types. In 2003, the International Commission on Illumination (Commission Internationale de L'Éclairage or CIE) defined 15 standard sky types, five categorized as clear, five as partial cloudy, and five as overcast skies. In several works, it was concluded that the CIE standard sky classification adequately represented empirical sky conditions [34–40]. Sky types of the same category have the same well-defined sky luminance patterns that easily yield the solar irradiance and daylight illuminance on the surfaces of interest through simple mathematical expressions [41]. Therefore, the CIE standard classification characterizes each type of sky in terms of energy and daylight. Figure 1 shows the main characteristics of each CIE standard sky type. Taking into account that illuminance (400–780 nm) and PAR (400–700 nm) share part of the spectrum of visible radiation, the use of the CIE Standard Classification is proposed in this work as the main parameter for characterizing the dependency of the Q_p/R_s ratio on atmospheric conditions.

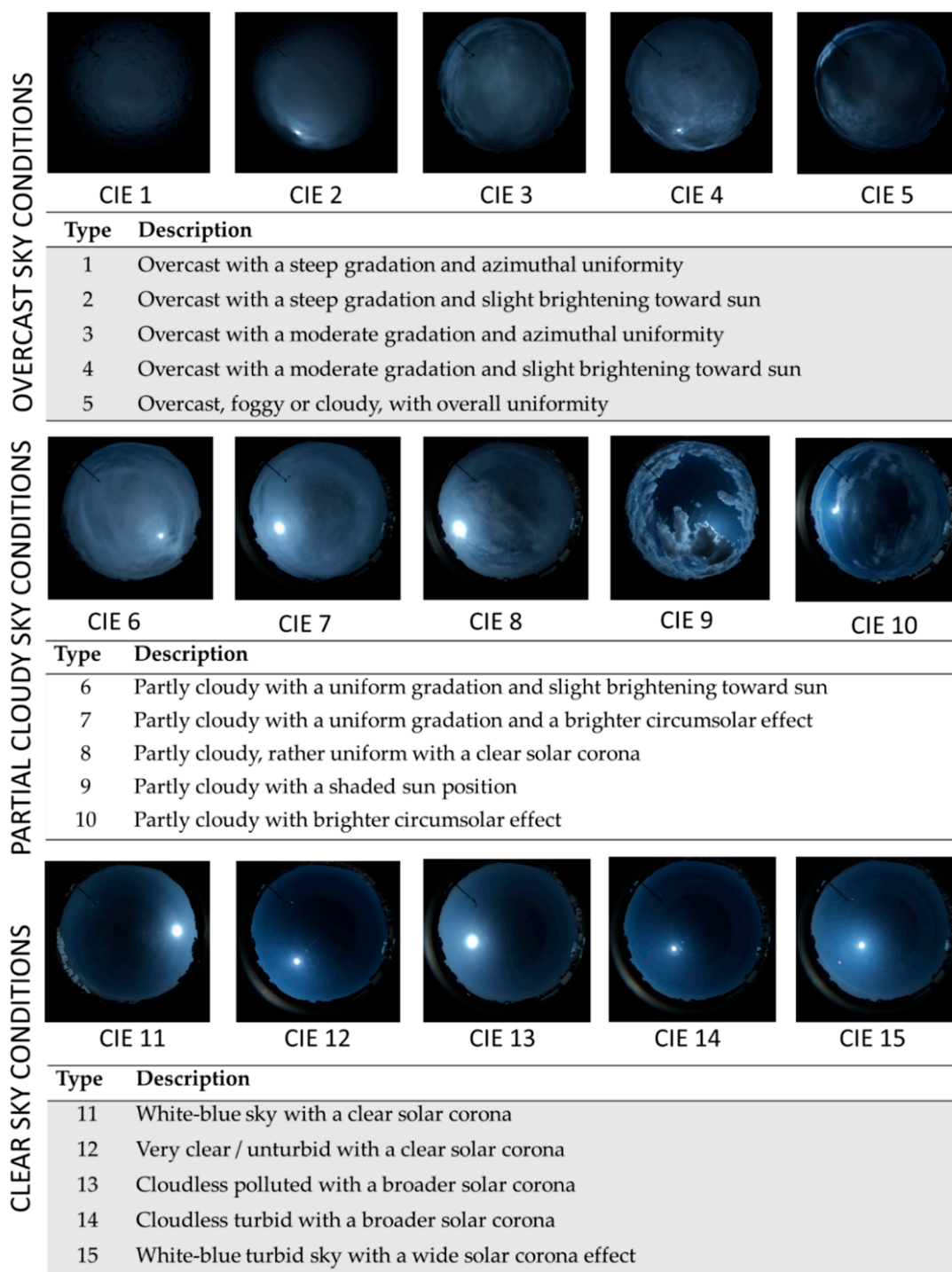


Figure 1. CIE Standard sky conditions. Images of different sky types recorded with a SONA201D All-Sky Camera—Day in Burgos, Spain.

The study is focused on the determination of the Q_p/R_s ratio in Burgos, Spain and its dependency on sky conditions. Experimental data on horizontal solar global irradiation, R_s ; photon photosynthetic flux density, Q_p ; and, the CIE standard classification for homogeneous skies; collected through experimental sky scanner measurements, were available for this work. A complete statistical analysis of the results over different temporal (ten-minute, hourly, daily, and monthly) phases was completed. The results collected under different sky conditions were tested in a 10-month experimental test campaign.

The paper will be structured as follows. The experimental facility and the measurement campaign as well the quality filters applied to the experimental data will be described in Section 2. The CIE Standard sky classification in Burgos during the experimental campaign will be introduced in Section 3. Temporal variability of the Q_p/R_s ratio over the different temporal intervals will be explained in Section 4. A variability analysis of the Q_p/R_s ratio in accordance with the CIE Standard Sky types will be analyzed in detail in Section 5. Finally, the main results and the conclusions of the study will be summarized in Section 6.

2. Experimental Data

The meteorological and radiometric weather station that recorded the experimental data for this study is located on the roof of the Higher Polytechnic School building (EPS) of Burgos University ($42^{\circ}21'04''$ N, $3^{\circ}41'20''$ W, 856 m above mean sea level). Figure 2 shows the location of the meteorological station on the flat roof of the EPS building, where the climatic parameters are measured: ambient temperature, relative humidity, atmospheric pressure, wind speed and direction, and rainfall. A complete description of the experimental facility and its location can be found in previous papers [33,42].

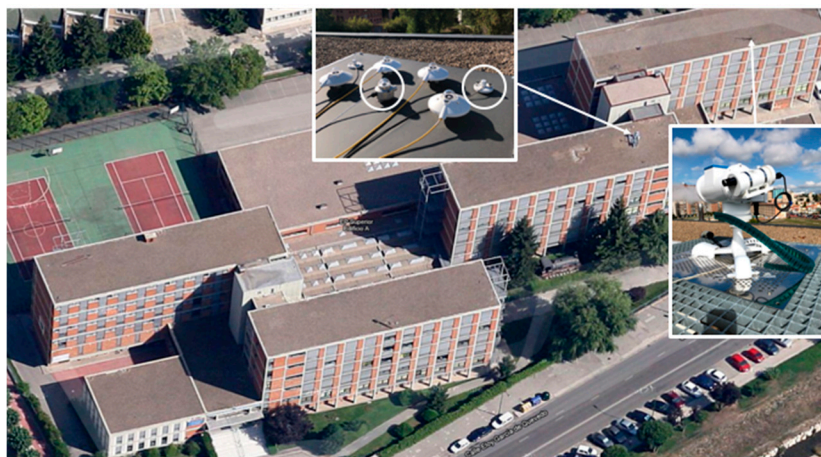


Figure 2. Location of the experimental equipment on the roof of the Higher Polytechnic School building at the University of Burgos, Spain.

Global horizontal irradiation, R_s data were measured by a pyranometer (model SR11, Hukseflux, Delft, The Netherlands,). An ML-020P photon meter was used to measure Q_p . The sky luminance and irradiance distribution were determined by a commercial MS-321LR sky scanner. Both instruments were manufactured by EKO Instruments (EKO Instruments Europe B.V., Den Haag, The Netherlands). The technical specifications of the various measurement instruments are shown in Tables 1–3.

Table 1. Sky scanner technical specifications.

Model	MS-321LR Sky Scanner
Dimensions (W × D × H)	430 mm × 380 mm × 440 mm
Mass	12.5 kg
FOV	11°
Luminance	0 to 50 kcd/m ²
Radiance	0 to 300 W/m ²
A/D Convertor	16 bits
Calibration Error	2%

Table 2. Pyranometer technical specifications.

Model	SR11
ISO classification	first class
Spectral range	300 to 2800 nm
Irradiance range	0 to 2000 W/m ²
Sensitivity	15 × 10 ⁻⁶ V/(Wm ⁻²)
Calibration uncertainty	<1.8%

Table 3. Photon-meter technical specifications.

Model	ML-020P
Measurement Range	0–3000 μmol·s ⁻¹ ·m ⁻²
Spectral range	400 to 700 nm
Operating temperature	–10 °C to 50 °C
Temperature response	±1%
Sensitivity	0.15 × 10 ⁻⁶ V/μmol·s ⁻¹ ·m ⁻²

Broadband solar irradiance, R_s , and photosynthetic photon flux density data, Q_p , were recorded every 10 min (recorded scans of 30 s on average). Experimental data were analyzed and then filtered using conventional quality criteria [43]. The sky scanner was adjusted on a monthly basis for taking measurements from sunrise to the sunset. It completed a full scan in four minutes and started a new scan every 10 min. The first and last measurements of the day ($\alpha_s \leq 7.5^\circ$) were discarded, as well as measurements higher than 50 kcd·m⁻² and lower than 0.1 kcd·m⁻², following the specifications of the equipment. If a data set (R_s , Q_p , or sky scanner measurement) failed to pass the quality criteria, then all the simultaneous data sets were rejected.

The experimental campaign ran between 1 April 2019 to 31 January 2020, during which time 20,631 data sets were collected, 18% of which were rejected after failing the quality criteria test. Therefore, the total data set comprised 16,937 ten-minute samples of R_s , Q_p , and the CIE Standard sky classification data sets.

3. CIE Standard Sky Classification in Burgos between 1 April 2019 and 21 January 2020

The Normalization Ratio (NR) introduced by Littlefair [44,45] in the original Standard Sky Luminance Distribution (SSLD) method [46], detailed and described in a previous paper [42], was used to determine the CIE standard sky types over Burgos between April 2019 and January 2020. The Frequency of Occurrence (FOC, %) of each sky type during the period under study is shown in Figure 3. As can be seen, all types of CIE standard skies can be found in Burgos. Sky types 11, 12, and 13, corresponding to CIE standard clear sky categories, had FOCs of around 10% (sky type 11) and 14.5% (sky types 12 and 13), followed by sky type 14 (FOC 8.4%). FOCs of around 7% were accounted for by sky types 1, 7, 8, and 15. The appearances of sky types 5, 9, and 10 were anecdotal in Burgos in the period under study, with FOCs of less than 3%. When only three sky categories were considered, the sky conditions in Burgos were predominantly clear, with FOCs of almost 62%, while the FOCs of overcast and partial cloudy conditions were 23.96% and 22.92%, respectively, as shown in Figure 4.

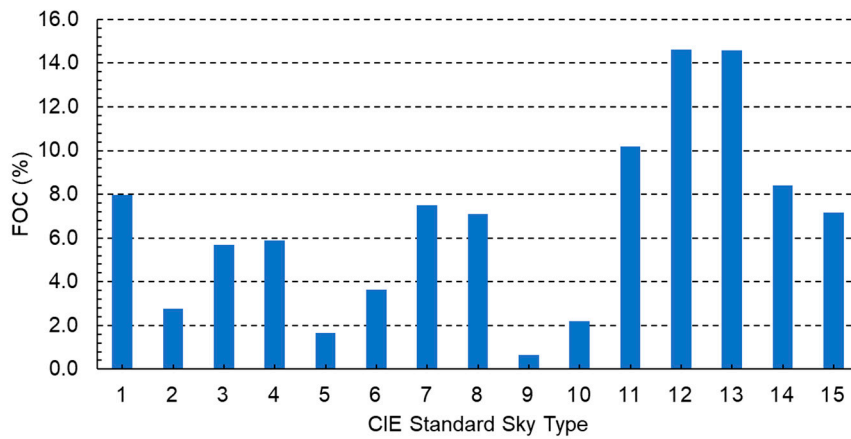


Figure 3. Frequency of occurrence (FOC, %) of CIE standard sky types in Burgos, Spain, between April 2019 and January 2020.

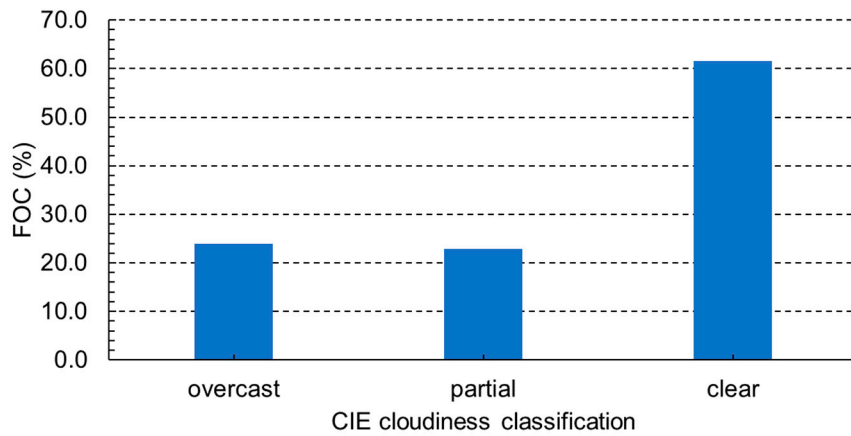


Figure 4. Frequency of occurrence (FOC, %) of CIE Cloudiness classification in Burgos, Spain, between April 2019 and January 2020.

Figure 5 shows that overcast sky conditions predominated in November and January and clear skies predominated from May to October in Burgos during the experimental campaign. Figure 6 reflects the predominance of clear skies in all hourly intervals of the day, from sunrise to sunset, at which point the standard CIE tends to classify the skies as partially overcast.

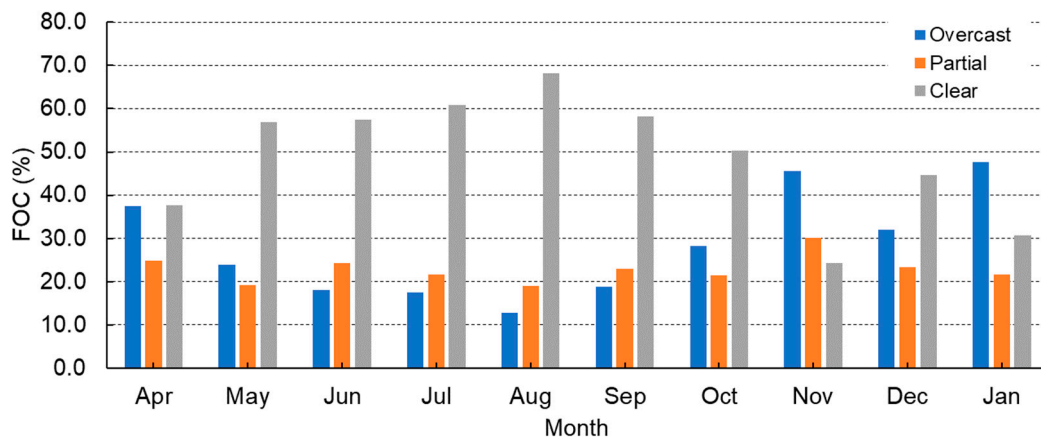


Figure 5. Monthly frequency of occurrence of clear, partial, and overcast sky conditions in Burgos between April 2019 and January 2020.

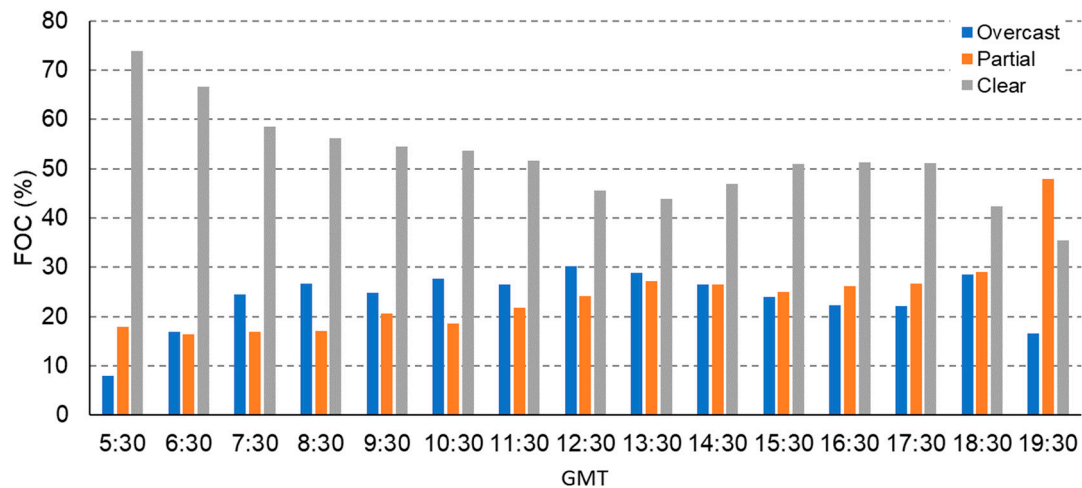


Figure 6. Daily frequency of occurrence of clear, partial, and overcast sky conditions in Burgos between April 2019 and January 2020.

4. Temporal Variability of the Q_p/R_s Ratio

The seasonal characteristics of the Q_p/R_s ratio were studied at differing intervals: ten-minute, hourly, daily and monthly. Figure 7 shows the high positive correlation between Q_p and R_s at ten-minute intervals ($R^2 = 0.992$) with a slope of $1.893 \pm 0.001 \mu\text{mol}\cdot\text{J}^{-1}$. This value is close to the mean value $1.93 \pm 0.15 \mu\text{mol}\cdot\text{J}^{-1}$, with a standard deviation of $\pm 0.15 \mu\text{mol}\cdot\text{J}^{-1}$. The Q_p/R_s ratio had similar values to those reported by other researchers [15], ranging between 1.21 and $2.84 \mu\text{mol}\cdot\text{J}^{-1}$.

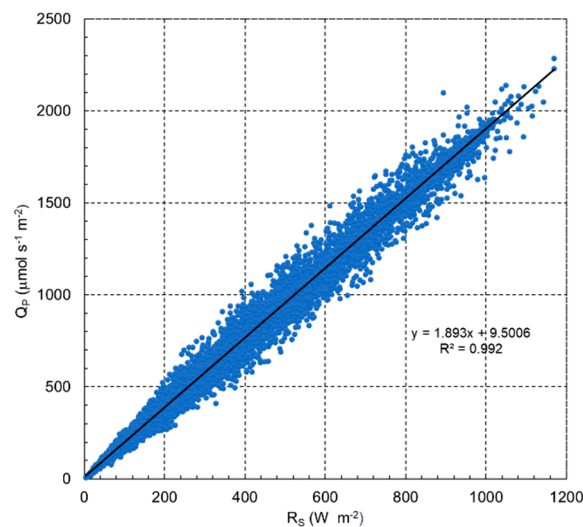


Figure 7. Photosynthetic photon flux density, Q_p ($\mu\text{mol}\cdot\text{s}^{-1}\cdot\text{m}^{-2}$), and broadband solar irradiance, R_s ($\text{W}\cdot\text{m}^{-2}$), measured in Burgos, between April 2019 and January 2020.

Figure 8 shows the box-plot of the mean hourly values of the Q_p/R_s ratio, calculated from the average of the ten-minute data, from sunrise to sunset, using the whole data base. The graph represents the mean value, the median, the three quartiles and both the maximum and the minimum values of the data, as well as the outlier values. Rising in the early hours of the day, Q_p/R_s stabilized in the central hours and tended to decrease at sun set. Higher dispersion of the values in the first and last hours than in the central hours of the day may be observed, as the interquartile range shows. The standard deviation ranged from $0.11 \mu\text{mol}\cdot\text{J}^{-1}$ within the hourly interval starting at 7:00 to $0.17 \mu\text{mol}\cdot\text{J}^{-1}$, within the hourly interval starting at 14:00. The average values were higher than the median values in all hours of the day except for the hourly interval starting at 06:00. The hourly average of the

ratio was $1.910 \pm 0.016 \mu\text{mol}\cdot\text{J}^{-1}$, with maximum and minimum values of $1.98 \pm 0.11 \mu\text{mol}\cdot\text{J}^{-1}$ and $1.75 \pm 0.16 \mu\text{mol}\cdot\text{J}^{-1}$, respectively, at 07:00 and at 19:00 h.

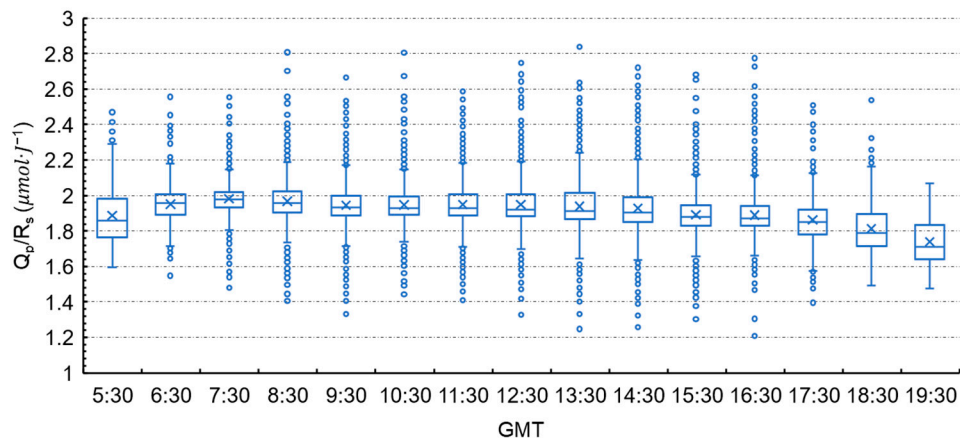


Figure 8. Box-plot of the hourly average of the ratio of photosynthetic photon flux density to broadband solar irradiance, Q_p/R_s . Blue crosses indicate the mean and blue lines inside the box, the median. The limits of the boxes give the 1st, 2nd, and 3rd quartiles, while the extreme whiskers are the minimum and the maximum points. Blue circles represent outliers.

Figure 9 presents the monthly values of the Q_p/R_s ratio calculated with the average of the ten-minute data, using the whole data base. Figure 8 shows that the monthly data were almost constant throughout the central months of the year, from May to October, with a standard deviation between 0.11 and 0.16 $\mu\text{mol}\cdot\text{J}^{-1}$, and an interquartile range between 0.10 and 0.15 $\mu\text{mol}\cdot\text{J}^{-1}$. November was the measurement campaign month with the highest data dispersion: the interquartile range was 0.24 $\mu\text{mol}\cdot\text{J}^{-1}$, with a standard deviation of 0.20 $\mu\text{mol}\cdot\text{J}^{-1}$. The maximum value was recorded in April ($1.98 \pm 0.15 \mu\text{mol}\cdot\text{J}^{-1}$), while the minimum was reached in December ($1.91 \pm 0.17 \mu\text{mol}\cdot\text{J}^{-1}$). The monthly average of Q_p/R_s was $1.930 \pm 0.025 \mu\text{mol}\cdot\text{J}^{-1}$. Based on the results of the monthly average of Q_p/R_s , some authors have suggested the existence of a seasonal dependence of this term. Alados et al. [4] recorded higher values in the summer months and lower values from November to January, in Granada, Spain. However, in Greece, Proutsos et al. [47] recorded the highest values for autumn (September) while the lowest averages (March) were recorded in spring, with intermediate values for summer and winter. In Midwestern US [48], the lower values with smaller deviations were recorded in the summer months while the winter months showed higher values of the ratio with larger deviations. In Lhasa (Tibetan Plateau), the ratio of photosynthetically-active to broadband solar radiation increased almost linearly from January to June and decreased until the end of the year in the same way [49]. In this study, slightly higher values were recorded in spring and autumn. The monthly average of the Q_p/R_s ratio was always above the median and the number of outliers above the maximum value was greater and had a higher absolute value than those below the minimum value.

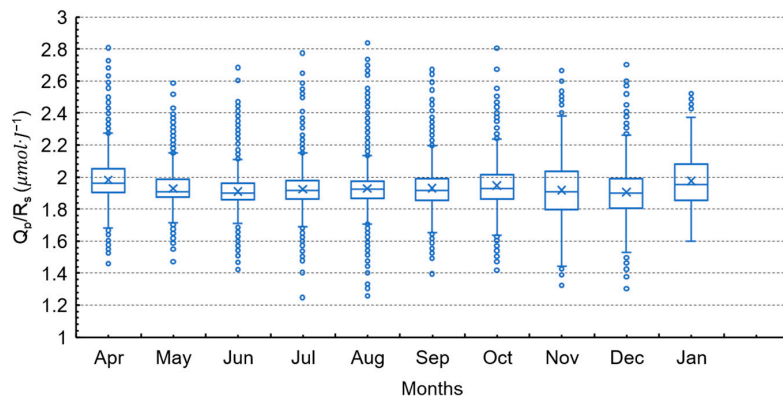
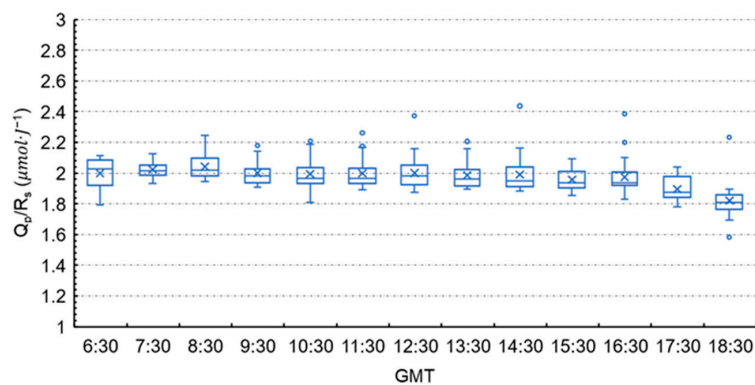
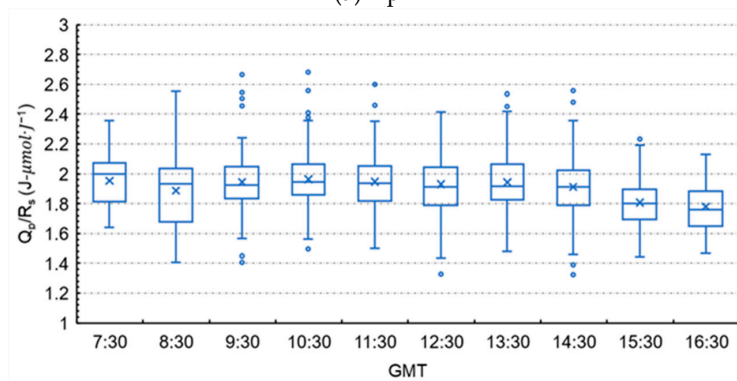


Figure 9. Box-plot of the monthly average of the photosynthetic photon flux density to broadband solar irradiance, Q_p/R_s , ratio.

A deeper analysis was conducted with the hourly values for the two months and the extreme values of the monthly averages of Q_p/R_s . Figure 10 shows the daily pattern of the hourly averages of the Q_p/R_s ratio, for April and November, including information on mean, median and variability through the quartile range. April presented higher and constant values throughout the day, decreasing in the last hours of the day, while November showed lower values of the ratio and more variability throughout the day. Both months presented similar patterns, with constant values of the Q_p/R_s ratio around noon, in a trend that decreased over the last few hours of the day. Apart from the differences in daily means, shown previously, there is also evidence of greater variability during November, mainly in the first hours of the day.



(a) April



(b) November

Figure 10. Daily pattern of the ratio photosynthetically-active photon flux density to broadband solar irradiance.

5. Variability of the Q_p/R_s Ratio with the CIE Standard Sky Types

Figure 11 shows the average photosynthetic photon flux density to broadband solar irradiance, Q_p/R_s , ratio, calculated on a ten minutes basis, for each CIE standard sky type. Clear sky types 12, 13, 14, and 15 showed smaller standard deviations (from 0.06 to 0.11 $\mu\text{mol}\cdot\text{J}^{-1}$) and a smaller interquartile range (from 0.05 to 0.09 $\mu\text{mol}\cdot\text{J}^{-1}$). However, the numbers of outliers were important for all these categories. The dispersion of the data within the categories corresponding to overcast and partial overcast skies was similar, with standard deviations between 0.15 $\mu\text{mol}\cdot\text{J}^{-1}$ (sky type 4) and 0.21 $\mu\text{mol}\cdot\text{J}^{-1}$ (sky type 9) and an interquartile range between 0.16 $\mu\text{mol}\cdot\text{J}^{-1}$ (sky types 3 and 4) and 0.21 $\mu\text{mol}\cdot\text{J}^{-1}$ (sky types 8 and 9). The highest values of the Q_p/R_s ratio were under CIE standard sky types 1, 2, 3, and 4; all categories of overcast sky conditions.

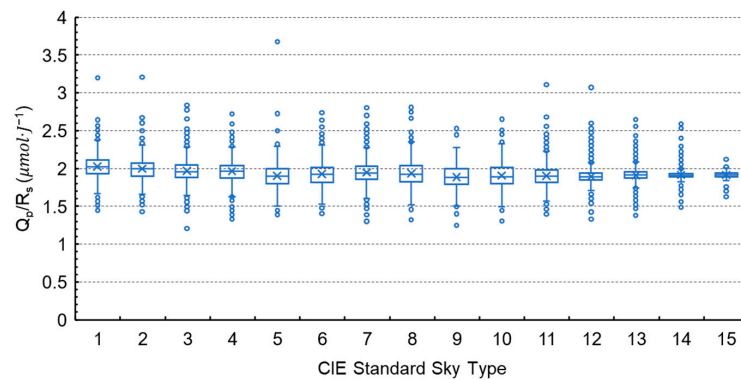


Figure 11. Box-plot ratio of photosynthetic photon flux density to broadband solar irradiance, Q_p/R_s , for each CIE standard sky type.

The categories of clear skies (CIE standard sky types from 11 to 15) showed the smallest values of the ratio. Sky types 5 and 9 presented an anomalous behavior. They are categorized as overcast and partial overcast categories, but the average values of the Q_p/R_s ratios for both sky types were closer to the values of clear sky categories. Furthermore, sky type 9 showed the smallest average value: $1.89 \pm 0.21 \mu\text{mol}\cdot\text{J}^{-1}$. The FOCs of both sky types, 5 and 9, were very scarce in the measurement campaign: 1.65% and 0.64%, respectively. CIE standard sky type 5, described as “overcast, foggy or cloudy, with overall uniformity”, presented high uniformity in terms of illuminance and broadband solar irradiance, as well sky type 9, described as “partly cloudy with a shaded sun position”.

When the 15 CIE standard sky types were reduced to three, (overcast, from sky types 1 to 5, partial, from sky type 6 to 10, and clear sky, from sky types 11 to 15), the average photosynthetic photon flux density to broadband solar irradiance ratio, Q_p/R_s , increased when sky cloudiness increased, as shown in Figure 12.

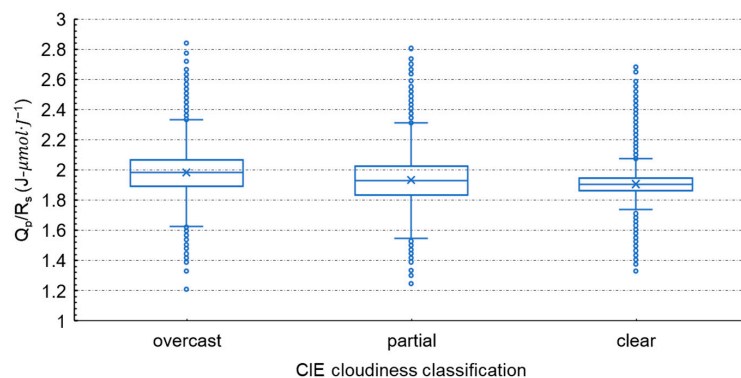


Figure 12. Box-plot of the ratio of photosynthetic photon flux density to broadband solar irradiance, Q_p/R_s , by CIE cloudiness sky classifications.

The average Q_p/R_s ratio for clear skies and for overcast skies was $1.90 \pm 0.11 \mu\text{mol}\cdot\text{J}^{-1}$ and $1.98 \pm 0.16 \mu\text{mol}\cdot\text{J}^{-1}$, respectively. Partial cloudy skies showed the highest dispersion of the data, with standard deviation and interquartile range values of 0.17 and $0.19 \mu\text{mol}\cdot\text{J}^{-1}$, respectively. However, the clear skies dataset had the largest number of outliers.

The Spearman correlation coefficient is a non-parametric measure of rank correlation, to determine the strength and direction of the relationship between two variables. If two datasets X and X' are strongly correlated, then the Spearman coefficient will be 1 (direct correlation) or if otherwise -1 (inverse correlation). Although $r(Q_p, CIE) = 0.56$ (p -value < 0.001) and $r(R_s, CIE) = 0.57$ (p -value < 0.001) both imply a moderate correlation, $(Q_p/R_s, CIE) = -0.23$ (p -value < 0.001). The p -value determine the significance of the results in relation to the null hypothesis (the results are due to random chance). The lower the p -value, the greater the statistical significance of the test and greater the confirmation of the hypothesis [50]. As the p -value was lower than 0.05 in all the tests, there was a statistically significant difference between the average Q_p/R_s ratios for each type of CIE sky, at a significance level of 5%.

When only three CIE categories were considered (clear = 3, partial = 2, and overcast = 1), $r(Q_p, CIE_{cloudiness}) = 0.52$ (p -value < 0.001) and $r(R_s, CIE_{cloudiness}) = 0.52$ (p -value < 0.001), and $(Q_p/R_s, CIE_{cloudiness}) = -0.22$ (p -value < 0.001). From these results, a weak relationship can be established between the value of the Q_p/R_s ratio and the CIE standard sky classification. However, previous results were confirmed in this research, in so far as the ratio of photosynthetic photon flux density to broadband solar irradiance, Q_p/R_s , presented its highest values over cloudy conditions and decreased with clear sky conditions, following the CIE Standard Sky classification as a reference for defining the sky conditions.

6. Conclusions

The analysis of photosynthetic photon flux density to broadband solar radiation ratios registered between April 2019 and January 2020 in Burgos, Spain, at ten-minute intervals, has shown a representative dependency on the sky type conditions classified by CIE taxonomy. The higher values of the Q_p/R_s ratio were for overcast sky types, while the values were lower and more dispersed under clear sky conditions.

Statistically significant differences have been found in the Q_p/R_s ratios for each CIE standard sky type. The overcast sky types presented the highest values of the ratio, with the clear sky categories presenting the lowest and most dispersed values. During the experimental campaign, there were only two exceptions to the expected behavior: sky types 5 and 9. They belonged to covered and partial covered sky type categories, respectively, presenting values closer to the clear sky categories according to the CIE standard. The main characteristic of both categories was a high uniformity in terms of illumination.

The higher dispersion of data corresponding to clear skies categories could be explained by the presence of aerosols or atmospheric turbidity, characteristics of clear sky types 13, 14 and 15, with FOC's 15%, 8% and 7% (Figure 3).

No seasonal dependency of Q_p/R_s can be established, as highlighted in this and the other studies that were reviewed, due mainly to the different sky conditions recorded during the experimental campaigns. As shown in Figure 5, between April 2019 to January 2020 in Burgos, Spain, clear skies predominated in summer, while in winter the overcast conditions presented the highest frequency of occurrence.

The analysis of the hourly values also revealed a daily pattern with higher and more stable values of Q_p/R_s in the first hours of the day that tended to stabilize around noon and to decrease around sunset. The study of the daily pattern of the sky types (clear, overcast and partial) show that, although clear skies are predominant at all hours of the day, the differences of the frequency of occurrence with respect to overcast and partially overcast skies decreases towards noon, as Figure 6 showed.

As has been demonstrated in this study and in others, the most influential factor in the Q_p/R_s value was the presence of overcast sky conditions. Although other authors used different climatological parameters for sky classification, the CIE Standard sky classification has proven itself to offer a good overall framework that can represent the sky conditions, covering the complete spectrum of sky categories.

Author Contributions: Conceptualization, M.D.-M. and C.A.-T.; methodology, A.G.-R. and S.G.-R.; software, A.G.-R.; validation, A.G.-R., M.D.-M.; formal analysis, A.G.-R. and S.G.-R.; investigation, A.G.-R. and S.G.-R.; original draft preparation, M.D.-M.; writing—review and editing, C.A.-T.; visualization, A.G.-R. and S.G.-R.; supervision, M.D.-M. and C.A.-T.; project administration, M.D.-M.; funding acquisition, C.A.-T. All authors have read and agreed to the published version of the manuscript.

Funding: This research was funded by Spanish Ministry of Science and Innovation, grant number RTI2018-098900-B-I00 and Consejería de Educación, Junta de Castilla y León, grant number BU021G19.

Conflicts of Interest: The authors declare no conflict of interest.

References

- McCree, K.J. The measurement of photosynthetically active radiation. *Sol. Energy* **1973**, *15*, 83–87. [\[CrossRef\]](#)
- Akitsu, T.; Kume, A.; Hirose, Y.; Ijima, O.; Nasahara, K.N. On the stability of radiometric ratios of photosynthetically active radiation to global solar radiation in Tsukuba, Japan. *Agric. For. Meteorol.* **2015**, *209–210*, 59–68. [\[CrossRef\]](#)
- Aguiar, L.J.G.; Fischer, G.R.; Ladle, R.J.; Malhado, A.C.M.; Justino, F.B.; Aguiar, R.G.; da Costa, J.M.N. Modeling the photosynthetically active radiation in South West Amazonia under all sky conditions. *Theor. Appl. Climatol.* **2012**, *108*, 631–640. [\[CrossRef\]](#)
- Alados, I.; Foyo-Moreno, I.; Alados-Arboledas, L. Photosynthetically active radiation: Measurements and modelling. *Agric. For. Meteorol.* **1996**, *78*, 121–131. [\[CrossRef\]](#)
- McCree, K.J. Test of current definitions of photosynthetically active radiation against leaf photosynthesis data. *Agric. Meteorol.* **1972**, *10*, 443–453. [\[CrossRef\]](#)
- Landsberg, J.J.; Waring, R.H. A generalised model of forest productivity using simplified concepts of radiation-use efficiency, carbon balance and partitioning. *For. Ecol. Manag.* **1997**, *95*, 209–228. [\[CrossRef\]](#)
- Kirk, J. Spectral Distribution of Photosynthetically Active Radiation in some South-eastern Australian Waters. *Mar. Freshw. Res.* **1979**, *30*, 81–91. [\[CrossRef\]](#)
- Pei, F.; Li, X.; Liu, X.; Lao, C. Assessing the impacts of droughts on net primary productivity in China. *J. Environ. Manag.* **2013**, *114*, 362–371. [\[CrossRef\]](#)
- Tsubo, M.; Walker, S. Relationships between photosynthetically active radiation and clearness index at Bloemfontein, South Africa. *Theor. Appl. Climatol.* **2005**, *80*, 17–25. [\[CrossRef\]](#)
- Moon, P. Proposed standard solar-radiation curves for engineering use. *J. Frankl. Inst.* **1940**, *230*, 583–617. [\[CrossRef\]](#)
- Monteith, J.L.; Reifsnnyder, W.E. Principles of Environmental Physics. *Phys. Today* **1973**, *27*, 51–52. [\[CrossRef\]](#)
- Szeicz, G. Solar radiation for plant growth. *J. Appl. Ecol.* **1974**, *11*, 617–636. [\[CrossRef\]](#)
- McCartney, H.A. Spectral distribution of solar radiation. II: Global and diffuse. *Q. J. R. Meteorol. Soc.* **1978**, *104*, 911–926. [\[CrossRef\]](#)
- Al-Shooshan, A.A. Estimation of photosynthetically active radiation under an arid climate. *J. Agric. Eng. Res.* **1997**, *66*, 9–13. [\[CrossRef\]](#)
- Foyo-Moreno, I.; Alados, I.; Alados-Arboledas, L. A new conventional regression model to estimate hourly photosynthetic photon flux density under all sky conditions. *Int. J. Climatol.* **2017**, *37*, 1067–1075. [\[CrossRef\]](#)
- Bai, J. Observations and estimations of PAR and solar visible radiation in North China. *J. Atmos. Chem.* **2012**, *69*, 231–252. [\[CrossRef\]](#)
- Hu, B.; Wang, Y.; Liu, G. Spatiotemporal characteristics of photosynthetically active radiation in China. *J. Geophys. Res. Atmos.* **2007**, *112*. [\[CrossRef\]](#)
- Meek, D.W.; Hatfield, J.L.; Howell, T.A.; Idso, S.B.; Reginato, R.J. Generalized relationship between photosynthetically active radiation and solar radiation. *J. Agron.* **1984**, *76*, 939–945. [\[CrossRef\]](#)
- Stanhill, G.; Fuchs, M. The relative flux density of photosynthetically active radiation. *J. Appl. Ecol.* **1977**, *14*, 317–322. [\[CrossRef\]](#)

20. Blackburn, W.J.; Proctor, J.T.A. Estimating photosynthetically active radiation from measured solar irradiance. *Sol. Energy* **1983**, *31*, 233–234. [[CrossRef](#)]
21. Stigter, C.J.; Musabilha, V.M.M. The conservative ratio of photosynthetically active to total radiation in the tropics (Dar es Salaam). *J. Appl. Ecol.* **1982**, *19*, 853–858. [[CrossRef](#)]
22. Rao, C.R.N. Photosynthetically active components of global solar radiation: Measurements and model computations. *Arch. Meteorol. Geophys. Bioclimatol. Ser. B* **1984**, *34*, 353–364. [[CrossRef](#)]
23. Harmel, T.; Chami, M. Estimation of daily photosynthetically active radiation (PAR) in presence of low to high aerosol loads: Application to OLCI-like satellite data. *Opt. Express* **2016**, *24*, A1390–A1407. [[CrossRef](#)] [[PubMed](#)]
24. Bat-Oyun, T.; Shinoda, M.; Tsubo, M. Effects of cloud, atmospheric water vapour and dust on photosynthetically active radiation and total solar radiation in a Mongolian grassland. *J. Arid Land* **2012**, *4*, 349–356. [[CrossRef](#)]
25. Escobedo, J.F.; Gomes, E.N.; Oliveira, A.P.; Soares, J. Modeling hourly and daily fractions of UV, PAR and NIR to global solar radiation under various sky conditions at Botucatu, Brazil. *Appl. Energy* **2009**, *86*, 299–309. [[CrossRef](#)]
26. Finch, D.A.; Bailey, W.G.; McArthur, L.J.B.; Nasitwitwi, M. Photosynthetically active radiation regimes in a southern African savanna environment. *Agric. For. Meteorol.* **2004**, *122*, 229–238. [[CrossRef](#)]
27. Jacovides, C.P.; Tymvios, F.S.; Assimakopoulos, V.D.; Kaltsounides, N.A. The dependence of global and diffuse PAR radiation components on sky conditions at Athens, Greece. *Agric. For. Meteorol.* **2007**, *143*, 277–287. [[CrossRef](#)]
28. Wang, L.; Gong, W.; Lin, A.; Hu, B. Analysis of photosynthetically active radiation under various sky conditions in Wuhan, Central China. *Int. J. Biometeorol.* **2014**, *58*, 1711–1720. [[CrossRef](#)]
29. Udo, S.O.; Aro, T.O. Global PAR related to global solar radiation for central Nigeria. *Agric. For. Meteorol.* **1999**, *97*, 21–31. [[CrossRef](#)]
30. Udo, S.O.; Aro, T.O. New empirical relationships for determining global PAR from measurements of global solar radiation, infrared radiation or sunshine duration. *Int. J. Climatol.* **2000**, *20*, 1265–1274. [[CrossRef](#)]
31. Jacovides, C.P.; Tymvios, F.S.; Papaioannou, G.; Asimakopoulos, D.N.; Theofilou, C.M. Ratio of PAR to broadband solar radiation measured in Cyprus. *Agric. For. Meteorol.* **2004**, *121*, 135–140. [[CrossRef](#)]
32. Alados, I.; Olmo, F.J.; Foyo-Moreno, I.; Alados-Arboledas, L. Estimation of photosynthetically active radiation under cloudy conditions. *Agric. For. Meteorol.* **2000**, *102*, 39–50. [[CrossRef](#)]
33. Suárez-García, A.; Díez-Mediavilla, M.; Granados-López, D.; González-Peña, D.; Alonso-Tristán, C. Benchmarking of meteorological indices for sky cloudiness classification. *Sol. Energy* **2020**, *195*, 499–513. [[CrossRef](#)]
34. Alshaibani, K. Finding frequency distributions of CIE Standard General Skies from sky illuminance or irradiance. *Light. Res. Technol.* **2011**, *43*, 487–495. [[CrossRef](#)]
35. Li, D.H.W.; Cheung, G.H.W. Average daylight factor for the 15 CIE standard skies. *Light. Res. Technol.* **2006**, *38*, 137–152. [[CrossRef](#)]
36. Li, D.H.W.; Lam, T.N.T.; Cheung, K.L.; Tang, H.L. An analysis of luminous efficacies under the CIE standard skies. *Renew. Energy* **2008**, *33*, 2357–2365. [[CrossRef](#)]
37. Li, D.H.W.; Tang, H.L.; Wong, S.L.; Tsang, E.K.W.; Cheung, G.H.W.; Lam, T.N.T. Skies classification using artificial neural networks (ANN) techniques. In Proceedings of the 6th International Conference on Indoor Air Quality, Ventilation and Energy Conservation in Buildings: Sustainable Built Environment, IAQVEC 2007, Sendai, Japan, 28–31 October 2007; pp. 61–68.
38. Torres, J.L.; de Blas, M.; García, A.; Gracia, A.; de Francisco, A. Sky luminance distribution in Pamplona (Spain) during the summer period. *J. Atmos. Sol. Terr. Phys.* **2010**, *72*, 382–388. [[CrossRef](#)]
39. Torres, J.L.; de Blas, M.; García, A.; Gracia, A.; de Francisco, A. Sky luminance distribution in the North of Iberian Peninsula during winter. *J. Atmos. Sol. Terr. Phys.* **2010**, *72*, 1147–1154. [[CrossRef](#)]
40. Tregenza, P.R. Analysing sky luminance scans to obtain frequency distributions of CIE Standard General Skies. *Light. Res. Technol.* **2004**, *36*, 271–279. [[CrossRef](#)]
41. Li, D.H.W.; Chau, N.T.C.; Wan, K.K.W. Predicting daylight illuminance and solar irradiance on vertical surfaces based on classified standard skies. *Energy* **2013**, *53*, 252–258. [[CrossRef](#)]

42. Suárez-García, A.; Granados-López, D.; González-Peña, D.; Díez-Mediavilla, M.; Alonso-Tristán, C. Seasonal characterization of CIE standard sky types above Burgos, northwestern Spain. *Sol. Energy* **2018**, *169*, 24–33. [[CrossRef](#)]
43. Gueymard, C.A.; Ruiz-Arias, J.A. Extensive worldwide validation and climate sensitivity analysis of direct irradiance predictions from 1-min global irradiance. *Sol. Energy* **2016**, *128*, 1–30. [[CrossRef](#)]
44. Littlefair, P.J. A comparison of sky luminance models with measured data from Garston, United Kingdom. *Sol. Energy* **1994**, *53*, 315–322. [[CrossRef](#)]
45. Littlefair, P.J. The luminance distributions of clear and quasi-clear skies. In Proceedings of the CIBSE National Lighting Conference, Cambridge, UK, 27–30 March 1994; pp. 267–283.
46. Kittler, R.; Perez, R.; Darula, S. A new generation of sky standards. In Proceedings of the Eighth European Lighting Conference, Amsterdam, The Netherlands, 11–14 May 1997; pp. 359–373.
47. Proutsos, N.; Liakatas, A.; Alexandris, S. Ratio of photosynthetically active to total incoming radiation above a Mediterranean deciduous oak forest. *Theor. Appl. Climatol.* **2019**, *137*, 2927–2939. [[CrossRef](#)]
48. Yu, X.; Guo, X. Hourly photosynthetically active radiation estimation in Midwestern United States from artificial neural networks and conventional regressions models. *Int. J. Biometeorol.* **2016**, *60*, 1247–1259. [[CrossRef](#)] [[PubMed](#)]
49. Peng, S.; Du, Q.; Lin, A.; Hu, B.; Xiao, K.; Xi, Y. Observation and estimation of photosynthetically active radiation in Lhasa (Tibetan Plateau). *Adv. Space Res.* **2015**, *55*, 1604–1612. [[CrossRef](#)]
50. Spiegel, M.R. *Estadística*, 3rd ed.; McGraw-Hill: Mexico city, Mexico, 2002.

Publisher’s Note: MDPI stays neutral with regard to jurisdictional claims in published maps and institutional affiliations.



© 2020 by the authors. Licensee MDPI, Basel, Switzerland. This article is an open access article distributed under the terms and conditions of the Creative Commons Attribution (CC BY) license (<http://creativecommons.org/licenses/by/4.0/>).